Early Tumor Development Captured Through Nondestructive, High Resolution Differential Phase Contrast X-ray Imaging

A. Beheshti[a], **B. R. Pinzer**[b], **J. T. McDonald**[a], **M. Stampanoni**[b,c], and **L. Hlatky**[a,1]

[a]Center of Cancer Systems Biology, GRI, Tufts University School of Medicine, Boston, Massachusetts [b]Swiss Light Source, Paul Scherrer Institute, 5232 Villigen-PSI, Switzerland [c]Institute of Biomedical Engineering, ETH Zurich, 8092, Zurich, Switzerland

Abstract

Although a considerable amount is known about molecular dysregulations in later stages of tumor progression, much less is known about the regulated processes supporting initial tumor growth. Insight into such processes can provide a fuller understanding of carcinogenesis, with implications for cancer treatment and risk assessment. Work from our laboratory suggests that organized substructure emerges during tumor formation. The goal here was to examine the feasibility of using state-of-the-art differential phase contrast X-ray imaging to investigate density differentials that evolve during early tumor development. To this end the beamline for TOmographic Microscopy and Coherent rAdiology experimenTs (TOMCAT) at the Swiss Light Source was used to examine the time-dependent assembly of substructure in developing tumors. Differential phase contrast (DPC) imaging based on grating interferometry as implemented with TOMCAT, offers sensitivity to density differentials within soft tissues and a unique combination of high resolution coupled with a large field of view that permits the accommodation of larger tissue sizes (1 cm in diameter), difficult with other imaging modalities.

INTRODUCTION

It now appears that initial stages of tumor growth may be characterized by a greater degree of tissue organization and substructure than is commonly recognized (1, 2). The classic example of such organized regulation of tumor substructure is the induction, early in cancer progression, of infiltrating vessels e.g., tumor angiogenesis (3). Tumor angiogenesis provides an intra-tumor vascular network supplying all tumor cells and connecting aggregates of these cells to the host's established vascular system. Formation of infiltrating tumor vasculature is critical for not only exchange of nutrients and waste products within the tumor itself, but serves as a direct routing for cancer cells to communicate with the entirety of the rest of the body (4). The angiogenesis process, ubiquitous in early tumor development, has become a pervasive tumor target, and anti-angiogenic therapies are used across a wide spectrum of tumor types (5–7). Further investigation into other facets of substructure emerging during initial tumor growth should augment understanding of carcinogenesis and expand the set of therapeutic tumor targets derived from early tumor developmental process, beyond angiogenesis and gene dysregulations in cancer cells. Investigations into developing gliomas have shown that indeed substructure changes as gliomas develop. In addition, detailed analysis of these substructural alterations, both with

[1]Address for correspondence: Center of Cancer Systems Biology, GeneSys Research Institute, 736 Cambridge St SEMC-CBR1, Boston, MA, 02135. Lynn.Hlatky@tufts.edu.

and without cancer therapeutics, have been found to be useful in predicting the eventual biological state of the tumor at an advanced stage (8). To this point, it has also has been reported that tumor budding structures occurring at early stages of colorectal carcinoma can impact lymph node metastasis (9). To date, the lack of technical ability to visualize subtle density alterations and compartmentalization within soft-tissue has thwarted progress in this direction.

Sufficiently detailed visualization of novel structural features, evolving both within the tumor and within the tumor/microenvironment interface during early tumor formation, has been difficult to achieve. Limited resolution, along with size constraints for the tumor/tissue imaged, are major obstacles that currently hinder advancement of these types of *in vivo* studies. The gold standard for analysis of intra-tumor compartmentalization, composition and substructural features remains microscopy techniques, particularly the use of immunohistochemical and immunofluorescent antibody stains on fixed serial tumor sections (10). Whole-body imaging techniques, i.e., magnetic resonance imaging (MRI), X rays, computed tomography (CT), etc., can cover the entire tissue and tumor, but these are limited in their resolution or sensitivity, respectively, with best case typically around $1 \times 1 \times 1$ mm (11–14). In a basic research environment microMRI devices are able to detect better resolution up to 20–40 μm for both *ex vivo* and *in vivo* (15, 16). Although this technique provides high resolution it remains limited by low spatial resolution. High spatial resolution is needed to detect tumor substructures that will be below 20 μm in size (17). The limits of current microMRI devices, which only allow observations of large vessels and macro tissue/ tumor differences at these scales, are now being pushed (15). Below the resolution limits for microMRI, signal for biological substructures of interest lose specificity (16–18).

To achieve the necessary sensitivity coupled with the high resolution and large field of view required to observe the formation of substructure within the entirety of a developing tumor, we turned to a relatively new technique, synchrotron based phase-sensitive X-ray tomography (19, 20), installed at the TOMCAT beamline of the Swiss Light Source, Switzerland (11, 14, 21) (Fig. 1). The superiority of this technique for our purpose, as compared to standard X-ray tomography, is that it does not measure the attenuation of X rays passing through the tissue sample, which would give negligible contrast for any soft tissue structural features, but instead is sensitive to the phase shift that is accumulated by the coherent X-ray beam. The advantage of this modality is found in the exceedingly high degree of contrast that results from even small density differentials within soft tissues. Such a high degree of contrast permits the identification of cellular compartmentalization and varied structural complexities within soft tissues, along with the identification of aberrant foci and pathological features at a micrometer-resolution that is characteristic for X-ray microscopes. To measure this phase shift, a grating interferometer together with a grating-stepping protocol was used (22). This approach resulted in a series of projection images taken while the sample under study, in this case the entire tumor tissue, is rotated between 0–180 degrees. For the projection images each pixel encodes the local phase gradient of the wave function accumulated along the projected line ending in that pixel. The back-projected images (12) thus yield a three-dimensional distribution of the (real part of the) refractive index, which allows the differentiation of anatomical or pathological features, with a pixel size of 7.4 μm. Even at such high resolution, the scanning and processing the image of our 1 cm diameter tumor/tissue, takes only about 4 h, as opposed to weeks with the more conventional image modalities (23).

METHODS

Cell Culture

Murine Lewis lung carcinoma (LLC) cells were obtained from American Type Culture Collection (Manassas, VA). Cells were cultured in DMEM, high glucose (Gibco Invitrogen Cell Culture, Carlsbad, CA) with 10% fetal bovine serum (FBS, Gibco Invitrogen Cell Culture), 5% $CO2$. Cells were passaged when at 80% confluence.

Tumor Implant and Collection for Imaging

Male C57BL/6 mice 8 weeks of age (Jackson Labs, Bar Harbor, ME) were used for *in vivo* studies. Subcutaneous LLC implantations, into the caudal portion of the back, were made in 9 replicate mice. Mice were monitored, with tumor size and animal weight measured daily. Three replicate tumors were collected for TOMCAT imaging at three different early time points. The first set of tumors were taken at the time the tumor was first detectable, referred to as T = 0, 3 days post-detection (T = 3) and 6 days post-detection (T = 6). In all cases the replicate tumor-bearing animals were sacrificed and tumors with surrounding normal tissue excised. To complement the TOMCAT imaging, full necropsy was performed at sacrifice. These tissue samples were prepared in 10% formalin, paraffin embedded and used as additional controls to match tissue used for TOMCAT imaging. For TOMCAT imaging the tumor samples including adjacent microenvironment tissue (tumor plus tissue were all <1 cm in diameter), were placed in 4% paraformaldehyde and the liquid was degassed prior to imaging. Only the T = 3 and T = 6 day samples were imaged at TOMCAT. After completion of differential phase contrast X-ray imaging, the tumor tissues were embedded in paraffin. Paraffin-embedded tissues were cut into 4 μm slices and stained with hematoxylin and eosin (H&E) (10).

Beamline and Tomographic Imaging

The grating interferometer setup as described by McDonald *et al.* (11) was used at an energy of 25 keV and at the second Lohmann distance, i.e., with an inter-grating distance of 120 mm. A 300 μm thick LuAG:Ce scintillator converted the X rays to visible light, which was captured by a CCD camera with 7.4 μm voxel size. It took an acquisition time of 450 ms to fill the chip with an effective dynamic range of 12 bit.

For mechanical fixation, the samples were embedded in an Eppendorf cylinder in a 2% wet agarose gel made with PBS. The Eppendorf was immersed in an "aquarium" filled with milliQ water to match the refractive index of the agarose gel embedding the sample. Five grating steps were used to scan two periods of the interference pattern, followed by Fourier component analysis to extract the shift of the stepping curves. The reference stepping curve without sample was calculated from 240 flat field images per grating step, and 1,080 projections were recorded for tomographic reconstruction. The total scan time (6,637 exposures + movement overhead) was about 1 h. A dose rate of 6.9 Gy/s is applied on the sample during imaging based on an approximate absorption of 22% and a photon flux of 7.8×10^{10} s^{-1} mm^{-1}. A total radiation dose of 2.5×10^4 Gy is estimated for a complete scan or tomograph at a voxel size of 7.4 μm. Since the samples are fixed no damage or radiation hardening has been observed with this study and past studies have shown a dose of 10^6 Gy is required to induce significant biological structural changes (11, 17, 24). For all data post-processing, a combination of in-house software (25) and open-source software was used (ImageJ software, ParaView).

RESULTS

Tumor Injections and Early Progression of Tumors

For the study presented here, a well-established and aggressive cancer cell line, murine Lewis lung carcinoma (LLC), was chosen. Anatomical development during early tumor growth was investigated. This carcinoma line was originally isolated from a spontaneous tumor formed in the lung and liver of C57BL/6 mice with subcutaneous tumors (26). The LLC cell line has since been characterized to have not only grown as localized tumors but to express metastatic properties (27). In this investigation LLC cells were injected subcutaneously in syngeneic C57BL/6 mice and monitored for the appearance of the first detectable tumor. The time at which the first tumor was observed is referred to as T = 0. Three and six days after the T = 0 point (T = 3 and T = 6), entire tumors still embedded in their surrounding nontumor microenvironmental tissue were collected. The average tumor sizes, given in Fig. 2b, show that the tumors at T = 0, referred to as "early", are relatively small (78.54 mm^3 ± 8.54 mm^3) compared to those often investigated, which typically are approximately 1,500 mm^3 or larger as reported in the literature (26–28). The T = 3 (214.21 mm^3 ± 80.33 mm^3) and T = 6 (535.22 mm^3 ± 117.72 mm^3) tumors, here considered middle and late time points, are again excised when smaller than typical sizes investigated, allowing us to probe the early tumor formation.

DPC Images and Image Processing of Early Tumor Formation

Individual H&E stained sections were made from the same tumors under study with TOMCAT to allow for correlation and calibration with the 3D TOMCAT reconstructed images. H&E images are shown for representative tumors from T = 0 (Fig. 2a), T = 3 (Fig. 2c) and T = 6 (Fig. 2f). As informative as H&E sections are, unfortunately, each section only captures a 2D rendering of a cross-sectional slice of the whole tumor/tissue. To reconstruct the full 3D architecture of the tumor and tumor/tissue interface by H&E slides would be inordinately time consuming and not cost effective (23). Currently research has been done comparing H&E images to MRI images, demonstrating the advantages and higher resolution of this technique compared to standard histology (29, 30). We here demonstrate similar comparisons (with better spatial resolution) using TOMCAT on whole excised tumors still encased in their surrounding tissue microenvironment. These tissues were imaged in approximately 4 h allowing tomographic reconstruction of any plane within the sample, as shown (Figs. 2 and 3). The full tissue architecture became visible once the tumor tissue was imaged using the differential phase contrast (DPC) X-ray imaging from TOMCAT (11, 14, 21). For each tumor replicate at the different time points an internal substructure was detected (Figs. 2 and 3). Slices from the DPC data set obtained from TOMCAT were matched to the H&E slices to correlate density differentials in DPC data with cellular staining in H&E (Fig. 2c, d, f, h). An example of a series of DPC images is shown in Fig. 2g. Comparison between H&E and DPC images provided a reference for physical assignment to the actual region of the tissue (shown in the gray scale bar in Fig. 2h). The DPC signal is proportional to the electron density in the tissue, while the absorption contrast depends on a combination of density and atomic number of the material (22, 31).

From the DPC images additional rendering (described in the Methods) is applied to the images to obtain the best representation of the tissue with pseudo-coloring for different gray scale values (Fig. 2e and i). We can observe from these pseudo-colored images, brighter colors corresponding to more dense tissue regions and darker colors corresponding to less dense tissue regions. Through visualization of the processed image slices, a 3D rendering is obtained and an overall image of the tumor is achieved (Fig. 3a and b). A novel feature of this technique was that it allowed examination of the entire tumor/tissue, in the case for T = 3 days a 3.9 mm in diameter (Fig. 3d), at a resolution that other nondestructive imaging

techniques currently lack. For example, microMRI techniques permit whole tissue imaging comparable with the images we have obtained, but DPC images have superior spatial resolution of 7.4 μm/pixel (with a maximum of 20 μm for microMRI), which allows for better detail when enlarging to a region of interest (17). Multiple views and 3D construction enables an investigator to get an optimal view of the tissue through this technique (Fig. 3c and d). It is this powerful three-dimensional capability together with the simplified sample manipulation, ensuring integrity of the sample and minimizing mechanical manipulation which could introduce deformation artifacts, that renders this method particularly promising for future cancer research.

Within these early tumor tissues variations in density were revealed that strongly suggest the formation of distinct substructures and cellular compartmentalization within the tumors. Tumor regions are clearly revealed in the DPC images when compared to the H&E images (tumor regions outlined in red in the H&E images of Fig. 2c and f). Other anatomical features are recognizable in the DPC images, such as skin (indicated by black arrows in Fig. 2c, d, f, h), which has a higher tissue density and fat (indicated by blue arrows in Fig. 2c, d, f, h), which has a lower tissue density. A tissue atlas associating gray scale values from DPC images to specific tissue types provided easy reference for identification of features from DPC images (Fig. 2g). An orthogonal view of one slice from each of the DPC images reveals distinct density changes for both T = 3 and T = 6 (density differentials outlined in red in Figs. 3a and b). It appears that during these early days, LLC tumor substructure is first forming and then resolving and at the T = 3 time point a well defined substructure has appeared (Fig. 3a). More defined time dependent substructures are observed at T = 3 than are seen at later tumor time points, T = 6 (Fig. 3b). This is made further apparent by enlarging the view for these features in the DPC images, and is consistent with what is seen in the H&E samples from the same tumors. These DPC images demonstrate at the early time points (T = 3), lower density patterns are scattered throughout the tumor tissue, while at later time points (T = 6) centralized, larger and higher density regions appear in the tumor (Fig. 3). The DPC images are sufficiently detailed and allow for the quantification of the size, morphology and number of substructures present as a function of time within the tumor.

DISCUSSION

To date, the literature demonstrates few examples of compartmental substructure in early tumor development. Preclinical brain tumor models have been used to obtain much of the limited experimental data stemming from these types of studies (8, 32, 33). Prastawa *et al.* used MRI to examine and compare meningiomas with malignant gliomas, crude differences were observed on the tumor boundaries and substructures were observed outside the white matter (13). For MRI, investigators have attempted to create a gray scale tissue atlas of tumor cell regions and the corresponding stromal compartments for brain tumors (13, 34). This permitted quick recognition of the specific regions throughout the image that were then correlated to specific tissue regions. Yet, the data gathered with these image modalities is limited in resolution (at best $1 \times 1 \times 1$ mm) compared to the superior detail that DPC images obtained through TOMCAT can achieve (13). Even with high precision basic research techniques using microMRI devices, which reach a resolution of 20–40 μm the spatial resolution is unable to view smaller objects and substructures in tissue (15, 17). Pinzer *et al.* have shown studying Alzheimer's disease that standard microMRI techniques do not provide the resolution necessary to view the amyloid plaques in the brain. They show that the DPC images obtained are able to obtain to a higher spatial resolution compared to microMRI, with a voxel size of $7.4 \times 7.4 \times 7.4$ or $3.7 \times 3.7 \times 3.7$ μm^2 for standard or local tomography (17). DPC imaging provides resolution in the size range that current research seems to indicate is appropriate for detection of the necessary substructure (8, 9, 23). Due to the high resolution of 7.4 μm/pixel and 3D reconstructions from thousands of individual

images, creating a density map of the tissue architecture observed from the DPC images has the potential to reveal more insight into carcinogenesis then what currently exists. Recent investigations indicate that the morphology of a tumor in the early stages has impact on the eventual biological state of tumors and can give clues to predict the aggressiveness of the tumor at later stages (1, 8, 9, 33). Understanding how specific morphologies at early stages of tumor development can impact later tumor development will provide valuable insight for detection, prognosis and therapeutics (8, 9). We presented here the first imaging of tumor samples using differential phase contrast X-ray imaging. The data obtained demonstrates the value this technique offers to elucidate the fundamental question of whether there is an organized substructure and anatomically recognizable niche developing during the early stages of tumor formation. These initial studies suggest there are emerging and resolving 3D substructures that accompany early tumor formation. These substructures can be detected by imaging done at TOMCAT, offering a window into the carcinogenesis process. Future work to refine the measurement of the density differentials within a tumor and its associated microenvironmental tissue will allow quantitative assessment of the time-dependent development of these anatomical features in the early tumor tissues. These same approaches should also allow gathering of high-resolution, large-scale tumor data over a short time that will augment currently available techniques for the assessment of progression and grade of tumors at later stages.

Acknowledgments

REFERENCES

1. Hahnfeldt, P. The Host Support Niche as a Control Point for Tumor Dormancy: Implications for Tumor Development and Beyond. In: Enderling, H.; Almog, N.; Hlatky, L., editors. Systems Biology of Tumor Dormancy. New York: Springer; 2013. p. 19-36.

2. Hahnfeldt P, Panigrahy D, Folkman J, Hlatky L. Tumor development under angiogenic signaling: a dynamical theory of tumor growth, treatment response, and postvascular dormancy. Cancer Res. 1999; 59:4770–4775. [PubMed: 10519381]

3. Folkman J, Hahnfeldt P, Hlatky L. Cancer: looking outside the genome. Nat Rev Mol Cell Biol. 2000; 1:76–79. [PubMed: 11413493]

4. Klement GL, Yip TT, Cassiola F, Kikuchi L, Cervi D, Podust V, et al. Platelets actively sequester angiogenesis regulators. Blood. 2009; 113:2835–2842. [PubMed: 19036702]

5. Denaro N, Russi EG, Colantonio I, Adamo V, Merlano MC. The role of antiangiogenic agents in the treatment of head and neck cancer. Oncology. 2012; 83:108–116. [PubMed: 22777379]

6. Jo J, Schiff D, Purow B. Angiogenic inhibition in high-grade gliomas: past, present and future. Expert Review Neurotherapeutics. 2012; 12:733–747.

7. Folkman J. Role of angiogenesis in tumor growth and metastasis. Semin Oncol. 2002; 29:15–18. [PubMed: 12516034]

8. Lee KC, Hall DE, Hoff BA, Moffat BA, Sharma S, Chenevert TL, et al. Dynamic imaging of emerging resistance during cancer therapy. Cancer Res. 2006; 66:4687–4692. [PubMed: 16651420]

9. Kye BH, Jung JH, Kim HJ, Kang SG, Cho HM, Kim JG. Tumor budding as a risk factor of lymph node metastasis in submucosal invasive T1 colorectal carcinoma: a retrospective study. BMC Surgery. 2012; 12:16. [PubMed: 22866826]

10. Lillie, RD. Histopathologic technic and practical histochemistry. 3rd ed.. New York: Blakiston Division; 1965.

11. McDonald SA, Marone F, Hintermuller C, Mikuljan G, David C, Pfeiffer F, et al. Advanced phase-contrast imaging using a grating interferometer. J Synchrotron Radiat. 2009; 16:562–572. [PubMed: 19535872]

12. Pfeiffer F, Bunk O, David C, Bech M, Le Duc G, Bravin A, et al. High-resolution brain tumor visualization using three-dimensional x-ray phase contrast tomography. Phys Med Biol. 2007; 52:6923–6930. [PubMed: 18029984]

13. Prastawa M, Bullitt E, Moon N, Van Leemput K, Gerig G. Automatic brain tumor segmentation by subject specific modification of atlas priors. Academic radiology. 2003; 10:1341–1348. [PubMed: 14697002]

14. Stampanoni, M.; Groso, A.; Isenegger, A.; Mikuljan, G.; Chen, Q.; Bertrand, A., et al. Developments in X-Ray Tomography V. In: Bonse, U., editor. Proceedings of the SPIE. San Diego, USA: 2006. 63180M63181-63114

15. Pathak AP, Kim E, Zhang J, Jones MV. Three-dimensional imaging of the mouse neurovasculature with magnetic resonance microscopy. PloS one. 2011; 6:e22643. [PubMed: 21818357]

16. Dassler K, Roohi F, Lohrke J, Ide A, Remmele S, Hutter J, et al. Current limitations of molecular magnetic resonance imaging for tumors as evaluated with high-relaxivity CD105-specific iron oxide nanoparticles. Investigative Radiol. 2012; 47:383–391.

17. Pinzer BR, Cacquevel M, Modregger P, McDonald SA, Bensadoun JC, Thuering T, et al. Imaging brain amyloid deposition using grating-based differential phase contrast tomography. NeuroImage. 2012; 61:1336–1346. [PubMed: 22450300]

18. van Rooden S, Maat-Schieman ML, Nabuurs RJ, van der Weerd L, van Duijn S, van Duinen SG, et al. Cerebral amyloidosis: postmortem detection with human 7.0-T MR imaging system. Radiology. 2009; 253:788–796. [PubMed: 19789230]

19. David C, Nohammer B, Solak HH, Ziegler E. Differential x-ray phase contrast imaging using a shearing interferometer. Applied Physics Letters. 2002; 81:3287–3290.

20. Momose A. Phase-sensitive imaging and phase tomography using X-ray interferometers. Opt Express. 2003; 11:2303–2314. [PubMed: 19471338]

21. Marone F, Hintermüller C, McDonald S, Abela R, Mikuljan G, Isenegger A, et al. X-ray Tomographic Microscopy at TOMCAT. Journal of Physics: Conference Series. 2009; 186:012042.

22. Weitkamp T, Diaz A, David C, Pfeiffer F, Stampanoni M, Cloetens P, et al. X-ray phase imaging with a grating interferometer. Opt Express. 2005; 13:6296–6304. [PubMed: 19498642]

23. Roberts N, Magee D, Song Y, Brabazon K, Shires M, Crellin D, et al. Toward routine use of 3D histopathology as a research tool. Am J Pathol. 2012; 180:1835–1842. [PubMed: 22490922]

24. Kirz J, Jacobsen C, Howells M. Soft X-ray microscopes and their biological applications. Quarterly Reviews Biophy. 1995; 28:33–130.

25. Marone F, Münch B, Stampanoni M. Fast reconstruction algorithm dealing with tomography artifacts. Proceedings of the SPIE. 2010; 7804:780410.

26. Sugiura K, Stock CC. Studies in a tumor spectrum. III. The effect of phosphoramides on the growth of a variety of mouse and rat tumors. Cancer Res. 1955; 15:38–51. [PubMed: 13231073]

27. Brodt P. Characterization of two highly metastatic variants of Lewis lung carcinoma with different organ specificities. Cancer Res. 1986; 46:2442–2448. [PubMed: 3697987]

28. Nian WQ, Chen FL, Ao XJ, Chen ZT. CXCR4 positive cells from Lewis lung carcinoma cell line have cancer metastatic stem cell characteristics. Mol Cell Biochem. 2011; 355:241–248. [PubMed: 21553023]

29. Bradley DP, Tessier JJ, Ashton SE, Waterton JC, Wilson Z, Worthington PL, et al. Correlation of MRI biomarkers with tumor necrosis in Hras5 tumor xenograft in athymic rats. Neoplasia. 2007; 9:382–391. [PubMed: 17534443]

30. Cho H, Ackerstaff E, Carlin S, Lupu ME, Wang Y, Rizwan A, et al. Noninvasive multimodality imaging of the tumor microenvironment: registered dynamic magnetic resonance imaging and positron emission tomography studies of a preclinical tumor model of tumor hypoxia. Neoplasia. 2009; 11:247–259. 242p following 259. [PubMed: 19242606]

31. Bech M, Jensen TH, Bunk O, Donath T, David C, Weitkamp T, et al. Advanced contrast modalities for X-ray radiology: Phase-contrast and dark-field imaging using a grating interferometer. Z Med Phys. 2010; 20:7–16. [PubMed: 20211422]

32. Charles N, Holland EC. The perivascular niche microenvironment in brain tumor progression. Cell Cycle. 2010; 9:3012–3021. [PubMed: 20714216]

33. Calabrese C, Poppleton H, Kocak M, Hogg TL, Fuller C, Hamner B, et al. A perivascular niche for brain tumor stem cells. Cancer Cell. 2007; 11:69–82. [PubMed: 17222791]

34. Konukoglu E, Clatz O, Menze BH, Stieltjes B, Weber MA, Mandonnet E, et al. Image guided personalization of reaction-diffusion type tumor growth models using modified anisotropic eikonal equations. IEEE transactions on medical imaging. 2010; 29:77–95. [PubMed: 19605320]
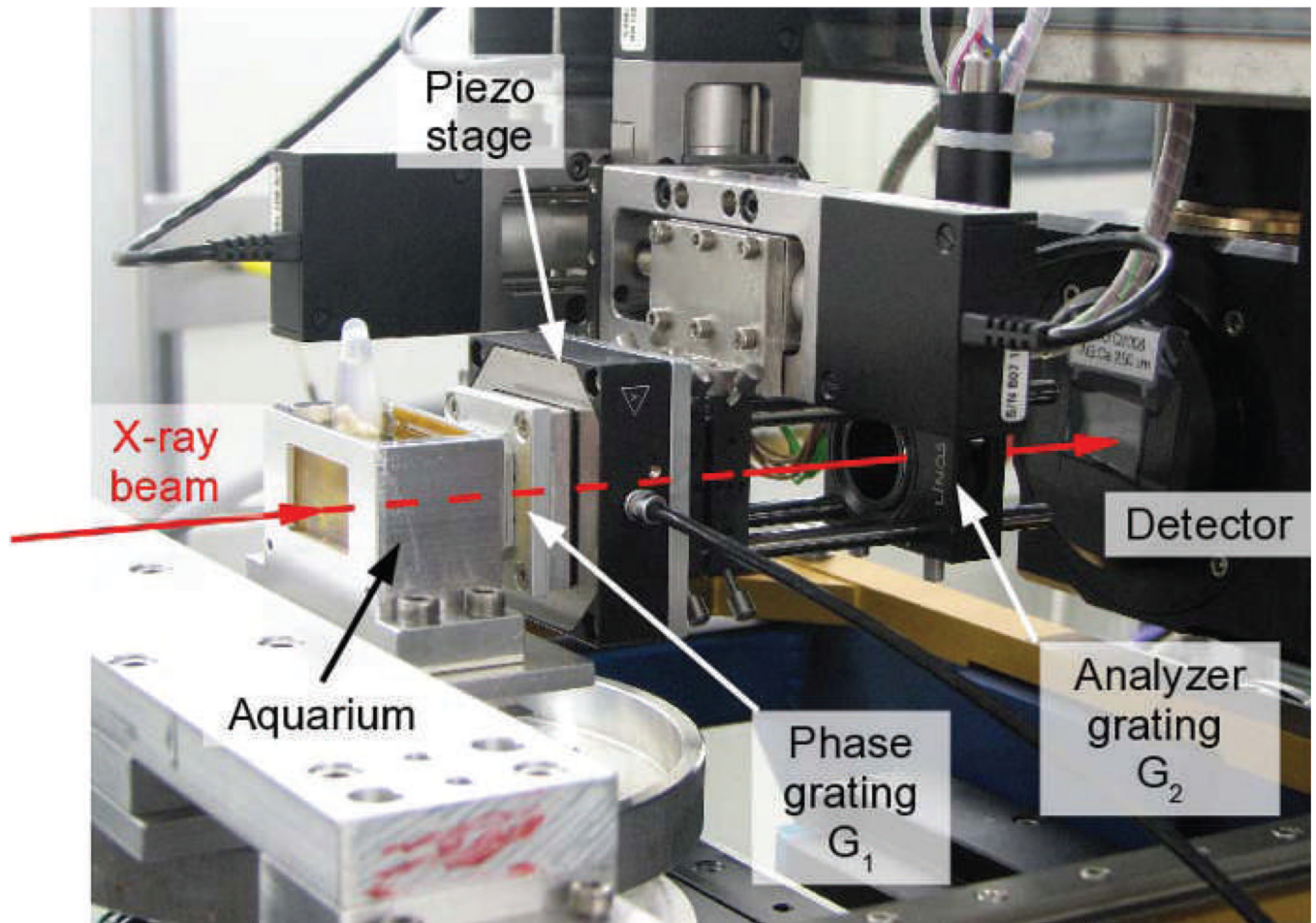
FIG. 1.
TOMCAT end-station with the grating interferometer setup for differential phase contrast imaging, as described by McDonald *et al*. (11). A container holding the samples is placed in phase-matching milliQ-water in the path of the X-ray beam (indicated by the redline arrow). The phase shift is measured with the grating interferometer together with a grating-stepping protocol (22). The piezo stage controls the grid translation for phase stepping, measuring the distribution of refraction angles imposed by the object being scanned.
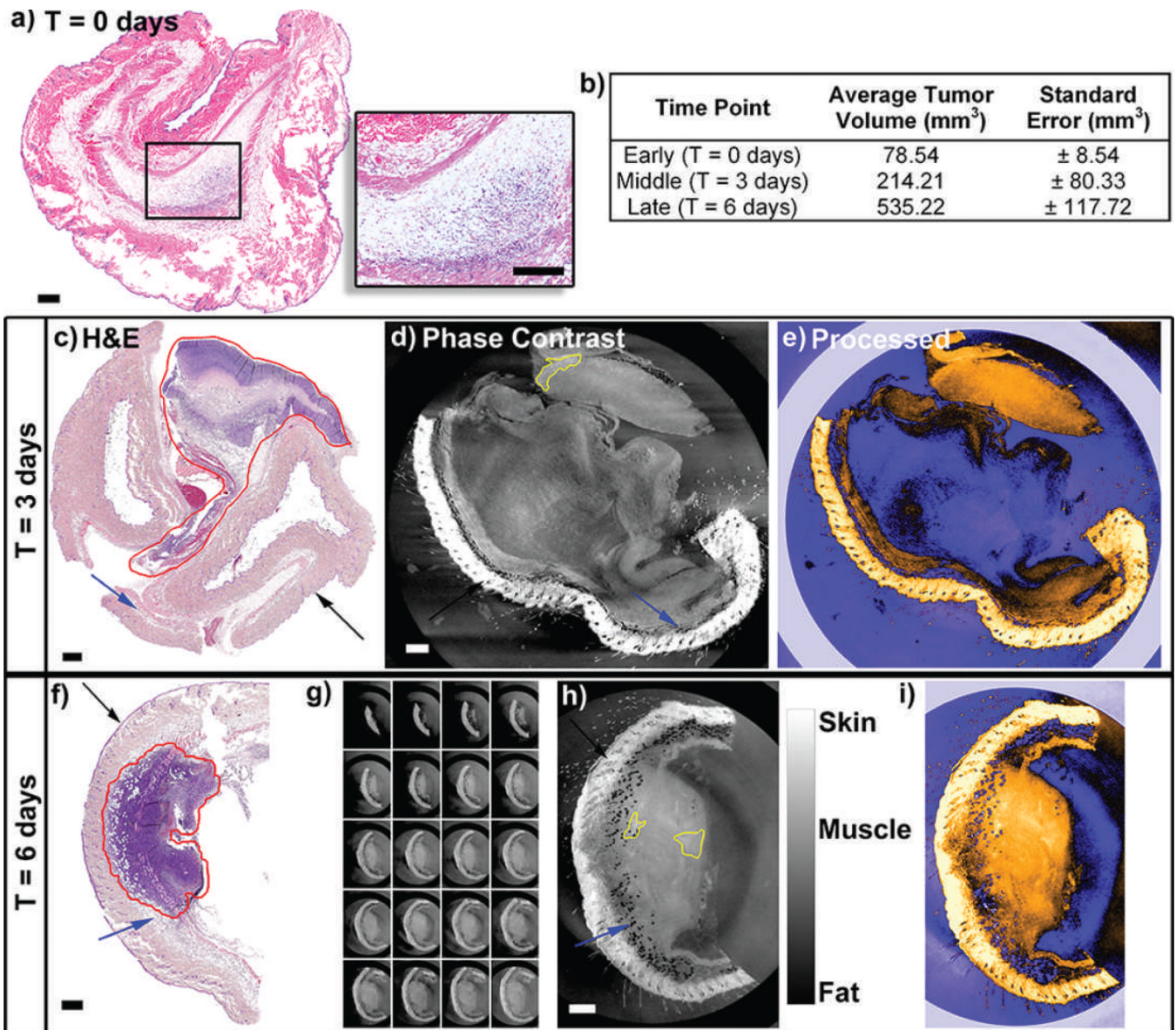
b)

Time Point	Average Tumor Volume (mm^3)	Standard Error (mm^3)
Early (T = 0 days)	78.54	± 8.54
Middle (T = 3 days)	214.21	± 80.33
Late (T = 6 days)	535.22	± 117.72

FIG. 2.

Representative H&E stained tumor sections and corresponding raw and rendered differential phase contrast X-ray images of the Lewis lung carcinoma (LLC) tumors sacrificed at different time points. All H&E images are a series of stitched images obtained with a 10× objective. Panel a: H&E of section of LLC tumor growing in C57BL/6 mouse sacrificed at the earliest time point, T = 0 days, when the tumor was first apparent. Panel b: The average tumor volumes for the tumors as a function of time point of sacrifice. Panel c: H&E of LLC tumor sacrificed at 3 days, T = 3 days after first measurable tumor, middle time point. The tumor area within the tissue is outlined in red. Considerable intra-tumor substructure is detected. Note, substantial regional differentials in H&E staining, with white, pink and purple banding, indicative of organization of cellular and nuclear material within the tumor boundary. Panel d: An image slice from the differential phase contrast (DPC) X-ray image obtained by TOMCAT for the same T = 3 day tumor as the H&E section of panel c. Panel e: Processed image providing a pseudo-color gradient based on density of tissue from the phase contrast images. Panel f: H&E of LLC tumor sacrificed at 6 days, T = 6, after first

measurable tumor, a late time point. As in panel c, the tumor area is outlined in red. The intra-tumor compartmentalization and substructure seen at T = 3 has now evolved and is resolving despite the fact the tumor has grown in size and infiltrated fat and muscle tissue. Panel g: A series of DPC images representing every 20 slices for the LLC tumor shown in panels f and h. Panel h: An image slice from the differential phase contrast (DPC) X-ray image obtained by TOMCAT for the same T = 6 day tumor as the H&E section of panel f. Yellow outlines enclose examples of substructure regions determined by density changes in the tissue. The black arrows point to the skin and blue arrows to the fat tissue. The gray scale bar depicts the range of gray values in the DPC images. Select tissue regions (fat, muscle and skin) have been associated with specific gray values in DPC images. Panel i: Processed image providing a pseudo-color gradient based on density of tissue from the phase contrast images. Scale bars are 500 μm.
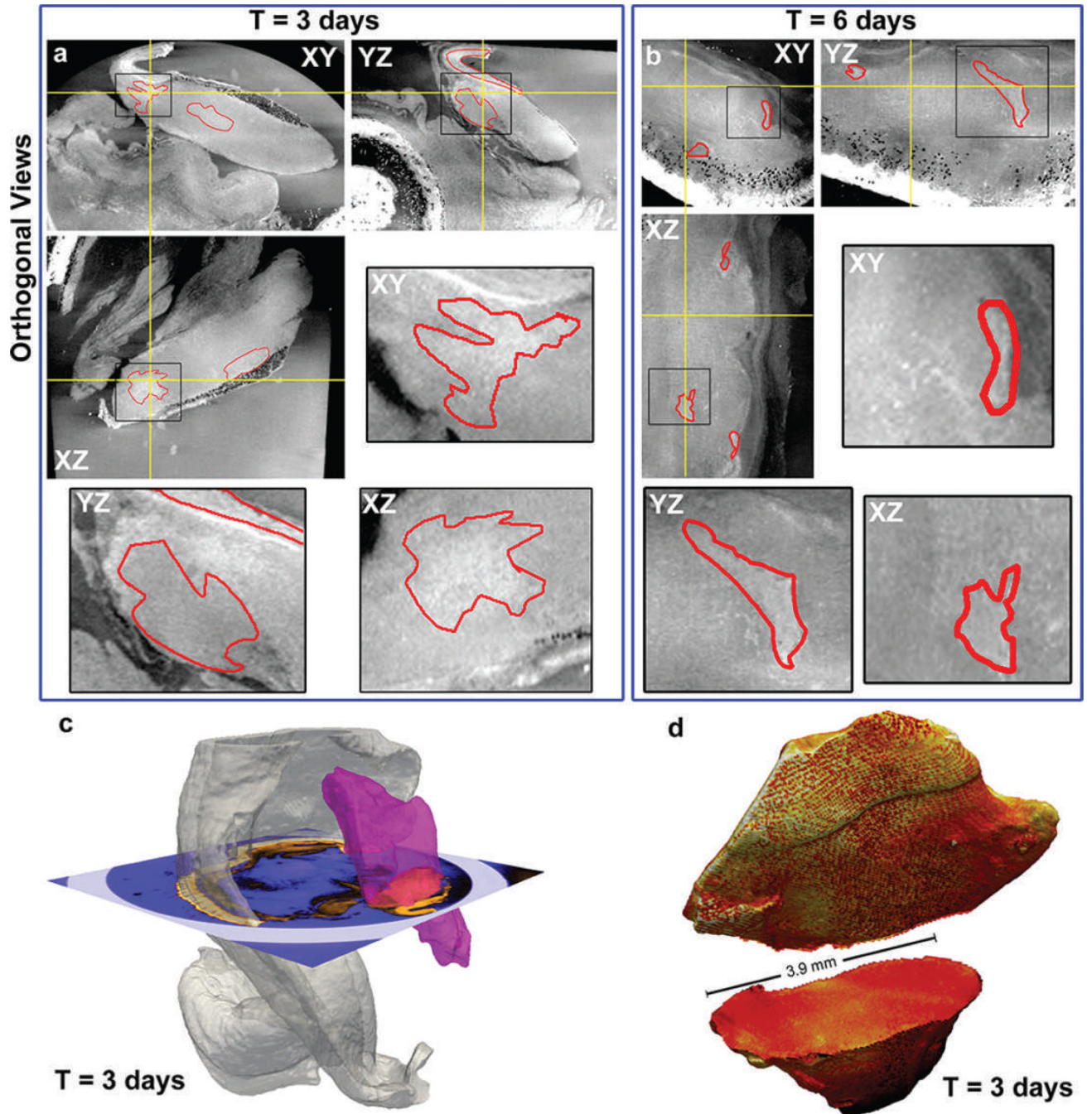
FIG. 3.
Representative differential phase contrast X-ray image and 3D processed image for LLC tumors. Panels a and b: Orthogonal views from an image slice of the DPC image. Red outlines enclose substructures determined by density changes in the tissues, with inserts providing enlarged views of these regions. Panel c: One method of 3D rendering with pseudo-coloring from the phase contrast images with slices from panels b and c within the tissue to indicate orientation of the slice for T = 3 days. Panel d: Close-up of the tumor as rendered from phase contrast images for T = 3 days, separating the tumor tissue from the attached adjacent microenvironment to highlight differential density structures within each tissue. Scale indicates the tumor diameter to be 3.9 mm.